

## Activated carbon from phenolic resin with controlled mesoporosity for an electric double-layer capacitor (EDLC)

Cite this: *J. Mater. Chem. A*, 2013, **1**, 6037

Chunhong Lei,<sup>a</sup> Negar Amini,<sup>b</sup> Foivos Markoulidis,<sup>a</sup> Peter Wilson,<sup>a</sup> Steve Tennison<sup>b</sup> and Constantina Lekakou<sup>\*a</sup>

Activated carbon materials are prepared from phenolic resin precursors by physical activation to fabricate electrodes for electric double-layer capacitors (EDLCs). Pore size and surface area of the carbon materials are controlled during the synthesizing process and after the carbonization through activation in a CO<sub>2</sub> atmosphere to different levels of burn-off. The resultant carbon materials were evaluated as EDLC electrodes, using electrochemical impedance spectroscopy (EIS) and galvanostatic charge–discharge (GCD) measurements with the organic electrolyte of spiro-(1,1′)-bipyrrolidinium tetrafluoroborate in propylene carbonate, SBPBF<sub>4</sub>/PC. The results of the study showed that the capacitance of carbon materials, as well as energy density of the EDLC cells, increased by increasing the level of burn-off (activation). The 46% activated carbon gave a capacitance of ~160 F g<sup>−1</sup> and an energy density of ~35 W h kg<sup>−1</sup>, at a current density of 1 mA cm<sup>−2</sup>. The long term cycling tests showed high cycling stability of these carbon materials.

Received 24th December 2012

Accepted 18th March 2013

DOI: 10.1039/c3ta01638b

www.rsc.org/MaterialsA

### 1 Introduction

Electrochemical double layer capacitors (EDLCs),<sup>1</sup> also known as supercapacitors or ultracapacitors, are fast energy storage and delivery devices, with power and energy densities performance between that of traditional dielectric capacitors which have high power output and batteries which have high energy storage. They can be used as alternative or complementary power sources in various applications including telecommunication devices, standby power systems, portable electronic devices and electric hybrid vehicles.<sup>2</sup>

Since EDLCs accumulate charges on high surface-area conducting materials such as activated carbon *via* the electrostatic force, no Faradaic reaction in the charge storage process is involved, so that supercapacitors often exhibit higher power capability and much higher recycle lifetime (>100 000 charge–discharge cycles) than rechargeable batteries. However, until now energy density of EDLCs has been only about one-tenth of the lowest density battery<sup>3,4</sup> and hence much of today's EDLC research is concerned with increasing its energy density with minimum sacrifice to power capability.<sup>5,6</sup>

Fabrication of advanced EDLC electrodes with novel materials plays a key part in elevating the specific energy storage

capacity of the EDLCs. Electrically conducting polymers and transition metal oxides like RuO<sub>2</sub> have been found to be promising electrode materials for supercapacitors of high energy density.<sup>6–9</sup> This is due to the high pseudo-capacitance effect these materials provide which implies that Faradaic redox reactions are involved in the energy storage processes. However, the lifetime and energy efficiency of these supercapacitors are limited due to the phase changes in the pseudo-capacitance materials and relatively slow redox reaction processes. Activated carbon<sup>10</sup> is the most commonly used material for electrodes in non-Faradaic EDLC devices due to carbon's high surface area (up to 2500 m<sup>2</sup> g<sup>−1</sup> (ref. 11)), chemical and temperature stability, relatively low cost and being environmentally friendly.

Activated carbons come from either natural sources or from carbonization of synthetic polymers. Natural sources, such as coconut shells and certain woods, are widely used for the production of activated carbons due to their low cost and abundance. Naturally derived carbon materials contain great amounts of impurities or ash, which can compromise the EDLC performance. In addition, the pore sizes are limited by what nature provides and may vary from source to source. Activated carbons obtained from synthetic sources, such as polymers, tend to be more expensive. However, highly porous carbons with well-controlled structures and a low amount of impurities can be obtained,<sup>12–14</sup> and have demonstrated excellent properties for energy related applications.<sup>15–17</sup> Phenolic resins have been shown to be very flexible precursors leading to high purity

<sup>a</sup>Department of Mechanical Engineering Sciences, Faculty of Engineering and Physical Sciences, University of Surrey, Guildford GU2 7XH, UK. E-mail: c.lekakou@surrey.ac.uk

<sup>b</sup>MAST Carbon International Ltd, Jays Close, Viabes Estate, Basingstoke, Hampshire RG22 4BA, UK

carbons and allowing the production of carbon materials with a wide range of pore structures.<sup>15,18</sup> Phenolic resin-based activated carbon fibres are reported to be promising electrode materials for high performance electrochemical supercapacitors.<sup>19,20</sup>

This report explores the application of activated carbon powders derived from phenolic resin in supercapacitor cells. Carbon in the form of powder is preferred for large scale coatings. Mesoporosity was introduced into the carbon materials by adding ethylene glycol as a pore former. In order to create microporosity in the carbons, the carbon materials were activated using CO<sub>2</sub> at high temperatures to various levels. Structures of the obtained carbon materials were analyzed and their electrochemical properties in EDLCs were characterized using electrochemical impedance spectroscopy (EIS) and galvanostatic charge-discharge (GCD) measurements. An organic electrolyte of spiro-(1,1')-bipyrrolidinium tetrafluoroborate in propylene carbonate (SBPBF<sub>4</sub>/PC) was used in this study. Compared with the common organic electrolyte of tetraethylammonium tetrafluoroborate in propylene carbonate (TEABF<sub>4</sub>/PC), the SBP cation has a smaller size of 0.4 nm than the TEA cation (0.7 nm), so it can easily diffuse into small micropores.<sup>21,22</sup> The solubility of SBP-BF<sub>4</sub> in PC is about 3 times higher than TEA-BF<sub>4</sub>, so that higher molar concentration is possible for SBP-BF<sub>4</sub>.

## 2 Experimental details

### 2.1 Carbon materials and characterization methods

Porous carbon materials used in this study were developed by MAST Carbon International.<sup>23</sup> To prepare these materials, phenolic resin was used as the carbon precursor and hexamine as the cross linking agent. Controlled mesoporosity was introduced into these carbons by addition of a pore former (ethylene glycol) prior to the curing step, the amount of which will decide the pore sizes. The resin cures at 150 °C and during curing a phase separation between the resin and the pore former occurs which eventually creates large interconnected pores in the carbon. After curing and washing out the ethylene glycol, the material was dried and then carbonized under a CO<sub>2</sub> flow at 800 °C using a 1 °C min<sup>-1</sup> heating rate. The carbon material was further activated under a CO<sub>2</sub> flow at 900 °C and different residence times. This leads to different levels of burn-off. All the carbon materials were milled and sieved to <75 µm particles for electrochemical tests.

Porous structures of the carbons were evaluated by the N<sub>2</sub> adsorption isotherms at 77 K, on a Micromeritics TriStar 3000. Prior to measurements all the samples were degassed at 250 °C for 2 h. The specific surface area of the samples was determined by the BET (Brunauer-Emmet-Teller) method<sup>24</sup> in the relative pressure range of 0.05–0.3. The micropore volume ( $V_{\text{mic}}$ ) was calculated according to the Dubinin-Radushkevich (DR) equation.<sup>25</sup> The volume of mesopores ( $V_{\text{mes}}$ ) was obtained by the difference between the total pore volume ( $V_{\text{tot}}$ ) measured at the relative pressure of 0.99 and  $V_{\text{mic}}$ . The pore size distribution (PSD) curves were calculated using the BJH (Barrett-Joyner-Halenda) method.<sup>26</sup>

The surface morphologies of the carbon materials were examined by scanning electron microscopy (SEM, Hitachi S4000) operating at 20 kV.

### 2.2 Fabrication of capacitors

Composite carbon electrodes were prepared from a blend of the activated carbon powder, acetylene carbon black (CB) (Alfa Aesar) and poly(vinylidene fluoride) (PVDF). All the chemicals were mixed at a weight ratio of AC : CB : PVDF = 90 : 5 : 5 in *N*-methyl-2-pyrrolidinone (NMP) to form a slurry. The slurry was then coated on an aluminium foil; the gap of the coating blade was adjusted so that a certain carbon loading was achieved for all the carbon materials. The coating was dried in an oven at 150 °C for 2 h. The final carbon loading was kept to ~5.5 mg cm<sup>-2</sup>. EDLC cells were fabricated using a symmetrical electrode configuration. A piece of cellulose paper (TF4060, Nippon Kodoshi Corp.) was used as a separator. The electrode working area was fixed to 2 cm<sup>2</sup> in all the devices. An organic solution (1.5 M SBP-BF<sub>4</sub>/PC, KKE-15, Japan Carlit Co., Ltd.) was used in the electrolyte system, which has an electrical conductivity of 16 mS cm<sup>-1</sup>.

### 2.3 Electrochemical characterization of capacitors

The performance of different EDLC cells was characterized by EIS and GCD tests, using a VersaSTAT MC analyser. The devices were characterized in a 2-terminal configuration; no reference electrode was used in the tests. During the electrochemical tests, a 2 kg weight was put on the body of EDLC cells to ensure a fixed gap between the two electrodes.

## 3 Results and discussion

### 3.1 Structural properties of the carbons

Porous carbon powders are denoted here according to their level of burn-off, *e.g.*, C-0, C-15, C-34, and C-46, representing carbons without any activation, with 15%, 34%, and 46% burn-off level, respectively. Textural characteristics of these carbons are shown in Table 1. It can be seen from the table that with increasing level of activation (burn-off), the specific surface area of the carbons, as well as their pore volume increased. The micropore structure (pores < 2 nm) of the carbon sample without any activation (C-0) is derived from the carbonization process where the high molecular weight domains convert to cross-linked spherical domains of high density glassy carbon, and decomposition of the low molecular weight matrix leads to the generation of microporosity.<sup>18</sup> From Table 1, it can be seen that the increment of micropore volume with the burn-off time (activation level) was faster than mesopore volume. The micropores contribute more to the surface area than

**Table 1** Textural characteristics of the phenolic resin-derived carbons

Carbon	$S_{\text{BET}}$ (m <sup>2</sup> g <sup>-1</sup> )	$V_{\text{tot}}$ (cm <sup>3</sup> g <sup>-1</sup> )	$V_{\text{mic}}$ (cm <sup>3</sup> g <sup>-1</sup> )	$V_{\text{mes}}$ (cm <sup>3</sup> g <sup>-1</sup> )
C-0	593	0.85 ± 0.09	0.28 ± 0.01	0.58 ± 0.08
C-15	820	1.03 ± 0.04	0.40 ± 0.02	0.63 ± 0.02
C-34	1083	1.28 ± 0.08	0.54 ± 0.03	0.74 ± 0.05
C-46	1600	1.84 ± 0.09	0.78 ± 0.04	1.06 ± 0.05

mesopores, as surface area of micropores per unit volume is larger than that of mesopores.

Activation of the carbons in carbon dioxide results in removing the low reactive glassy carbon nanoparticles further and creating some surface porosity in the nanoparticles.<sup>27</sup> Increasing the level of activation leads to increasing the micropore and mesopore volumes, as well as the surface area of the carbons. However, it does not affect the corresponding pore sizes significantly (Fig. 1). It can be seen from the pore size distribution (PSD) patterns in Fig. 1 that activation to a high level (46%) results in the displacement of the mesopore peak towards a smaller pore size. Nevertheless, mesopore PSD peaks for carbons without any activation and at different activation levels all appear at 20–30 nm. These mesopores are essential for transport of charges to the micropores and they are the major contributor to charge storage in the supercapacitor cells.<sup>28,29</sup>

Fig. 2(a) shows a SEM image of the surface of a coated carbon electrode. The amorphous region, like the one in the white square, is carbon black, which looks like chained beads. They tend to accumulate, possibly with polymer binder, around corners or between carbon particles where contact surface area is maximal. This certainly helps to decrease the contact resistance between carbon particles. Fig. 2(b) and (c) are magnified images of C-0 and C-46, taken on a smooth region of the carbon particle, like the one shown by the white circle in Fig. 2(a). It can be seen that the morphology of both of the carbon materials is a sol-gel structure, and no obvious change in surface morphology is observed by the activation due to the limited resolution of the SEM. As pores are formed between interconnected small spherical carbon domains of *ca.* 4 nm in size,<sup>18</sup> these pores are interconnected throughout the whole carbon bulk, and most of them have already existed before the activation. In the activation process, more pores are created between the hard particle networks and on the surface of the particles by etching away lower density regions. Interconnected mesopores play an important role in ensuring that charged ions can freely access all the surfaces due to better pore accessibility and less overlapping of the double layer structure. From this point of view, particle sizes of the carbon powders should be as small as possible to make full use of all the pores in a fast charge-discharge operation.

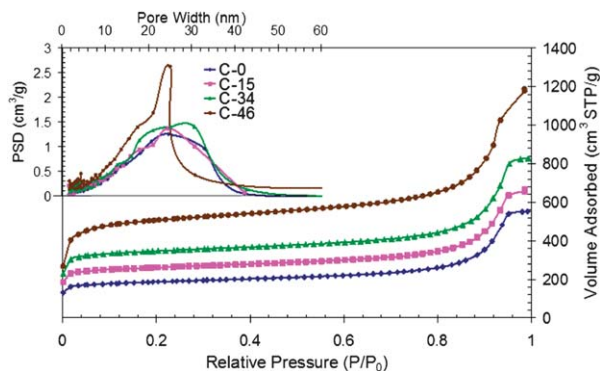


**Fig. 1** Nitrogen adsorption isotherms and the corresponding pore size distributions of the phenolic resin-derived carbons.

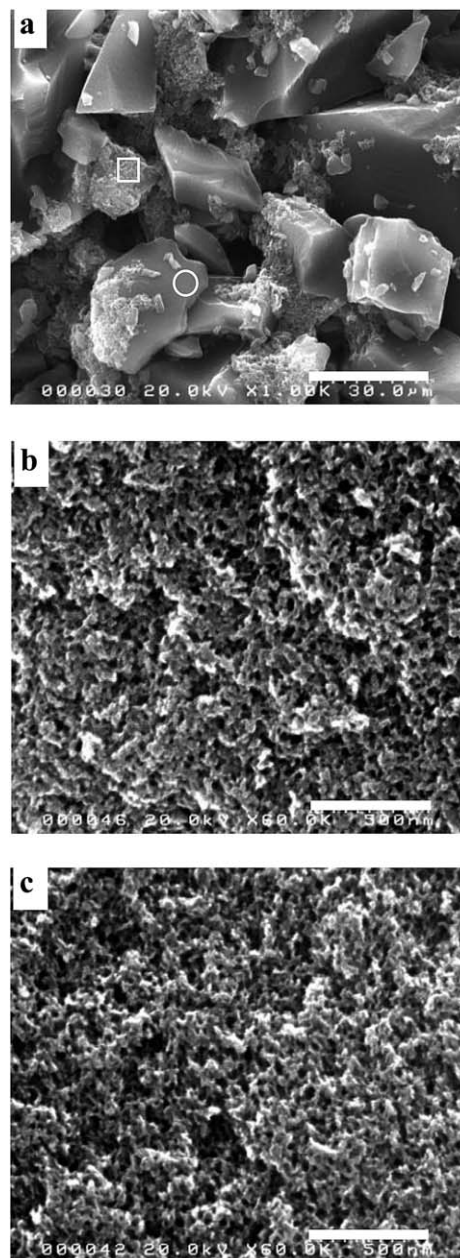


**Fig. 2** (a) SEM image of a coated carbon electrode surface at ×1k magnification, the scale bar corresponds to 30 μm; (b) SEM image of a C-0 carbon particle surface at ×60k magnification, the scale bar corresponds to 500 nm; (c) SEM image of a C-46 carbon particle surface at ×60k magnification, the scale bar corresponds to 500 nm.

### 3.2 Electrochemical performance

The EIS measurements on the cells were carried out at a DC bias of 0.2 V and a sinusoidal signal of 20 mV, over a frequency range from 1 MHz to 0.01 Hz.

Fig. 3(a) is the Nyquist plot from the EIS measurement on the four EDLC cells. The four curves were originally overlapping in this plot, as it is shown in the inset, and therefore for a clearer view, they have been separated by offsetting a small increment horizontally. They all show a nearly vertical straight line in the low frequency region, indicating typical behaviour of a supercapacitor.



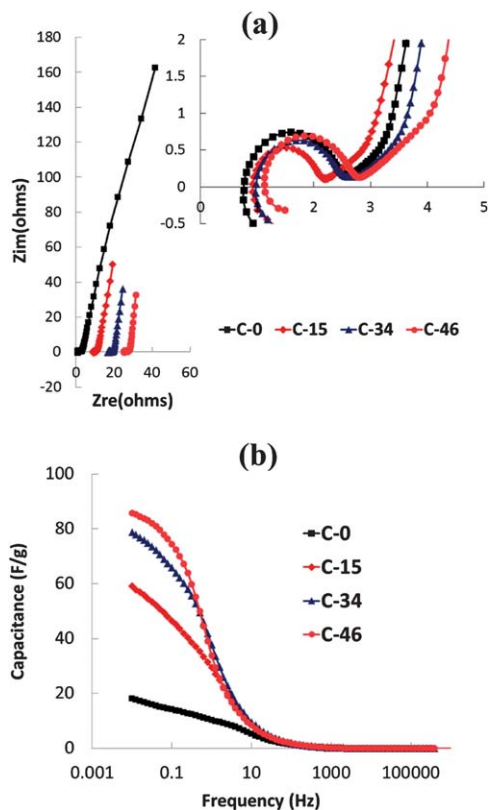


**Fig. 3** (a) Nyquist plots of EDLC cells with electrodes from C-0, C-15, C-34 and C-46 carbon materials, operating in SBPBF<sub>4</sub>/PC electrolyte. (b) Capacitance (F g<sup>-1</sup>) of the four carbon materials obtained from the EIS measurements.

At the high frequency region, above ~500 Hz, the semi-circles appeared, which correspond to electric resistance. They came mainly from carbon–Al contact resistance, as reported in our previous paper.<sup>30</sup> The length of the vertical region corresponding to the capacitance of the carbon electrodes decreased with increase in the level of activation. The capacitance of the carbon material in one electrode can be estimated by:

$$C = \frac{1}{\pi m f Z_{im}} \quad (1)$$

where  $f$  is the frequency,  $Z_{im}$  is the imaginary part of the impedance, and  $m$  is the mass of one electrode.

The capacitance *vs.* frequency curves are shown in Fig. 3(b). As can be seen, at the low frequency side (<10 Hz), the capacitance increased rapidly as the frequency decreased. At a certain frequency, the capacitance increased with the level of activation: C-0 < C-15 < C-34 < C-46. This increment became smaller as the level of activation increased, indicating that a higher level of activation is less effective to increase the capacitance. In the high frequency region (>10 Hz), capacitance values remain more stable; all carbon materials gave similar capacitance. This is because the deep and narrow pores cannot be penetrated by a highly alternating current.

GCD tests were carried out on the cells in a potential range of 0–3 V at various constant currents. Fig. 4(a) shows the plots of the GCD curve on the four cells with different carbon materials at 10 mA (~0.9 A g<sup>-1</sup>) current strength, operating in SBPBF<sub>4</sub>/PC electrolyte. The curves show a nearly triangular shape,

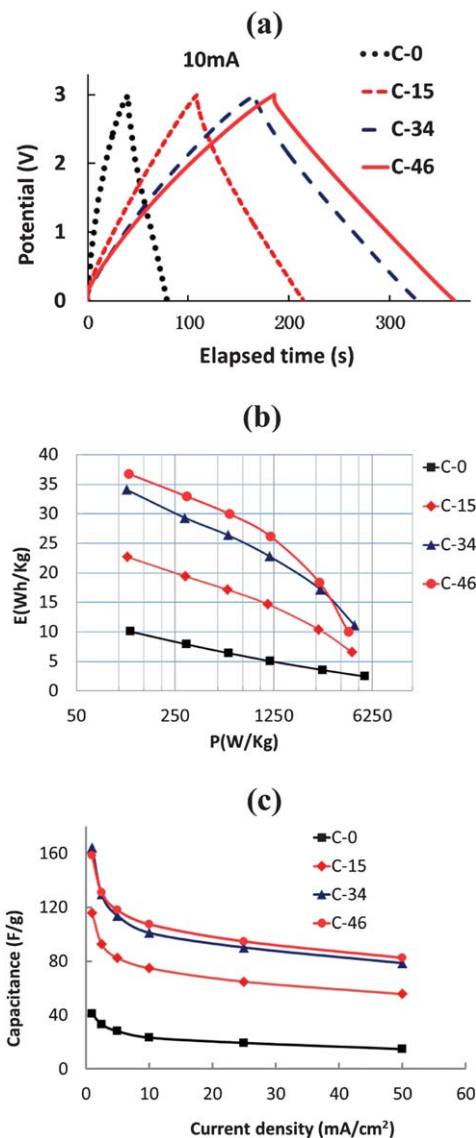


**Fig. 4** (a) GCD curve of the EDLC cells with C-0, C-15, C-34 and C-46 electrodes, in SBPBF<sub>4</sub>/PC electrolyte at a current of 10 mA; (b) Ragone plots of the four EDLC cells with SBPBF<sub>4</sub>/PC electrolyte; (c) plots of capacitance (F g<sup>-1</sup>) *vs.* current density (mA cm<sup>-2</sup>) of the four EDLC cells, obtained from the GCD measurements.

indicating a non-Faradaic process in the charge–discharge process and high energy efficiency. The internal resistance  $R_{int}$  can be determined from the  $IR$  drop at the initiation of a constant current discharge.<sup>31,32</sup> The  $R_{int}$  from  $IR$  drop did not change with the GCD current; they are ~2.4 Ω, 2.2 Ω, 1.8 Ω, and 2.2 Ω for the C-0, C-15, C-34, and C-46 electrodes, respectively.

From the discharge curve, the device specific energy density  $E$  and power density  $P$  can be obtained according to:<sup>33,34</sup>

$$E = I \int \frac{V dt}{2m} \quad (2)$$

$$P = \frac{E}{\Delta t_d} \quad (3)$$

where  $I$  is the constant current,  $m$  is the mass of one electrode (the current collector not included), and  $\Delta t_d$  is the time

elapsed during discharge. From this, the Ragone plot can be obtained.

The Ragone plot in Fig. 4(b) demonstrates that the energy density of the cells increases with increasing carbon activation level,  $C-46 > C-34 > C-15 > C-0$ , especially at the low power side. At the high power end, the energy density decreases with increasing power/current; all the curves tend to converge to the curve of C-0. The higher the activation level, the faster the decrease is. This indicates that the contribution of the increased surface area by activation to the capacitance is limited at large currents. This is reasonable, as the ratio of micro- to meso-pore surfaces at high activation levels is higher than that at low activation levels and adsorption-desorption of charges on micropores is more difficult than that on mesopores at large currents.

The mass-specific capacitance of one electrode was calculated from the discharge slopes of the charge-discharge cycles at different currents according to:

$$C = \frac{2I\Delta t}{m\Delta V} \quad (4)$$

where  $I$  is the constant current,  $m$  is the mass of one electrode (the current collectors not included), and  $\Delta t$  is the time elapsed during voltage change  $\Delta V$ . The calculated specific capacitances are plotted against current densities ( $\text{mA cm}^{-2}$ ) as shown in Fig. 4(c).

Unlike the capacitances obtained from EIS measurements where charge-discharge is very shallow, the capacitance obtained from the GCD discharge slope more or less reflects the real capacitance of the electrode materials. It can be seen from Fig. 4(c) that the drop-off of discharge capacitances with the current density larger than  $5 \text{ mA cm}^{-2}$  is not as steep as the energy densities in the Ragone plots. This is because the calculation of capacitances was from the linear parts of the discharging slopes and the  $IR$  drop at the beginning of discharging was not counted. As expected, the capacitance increases with the carbon activation level, the increment from C-0 to C-15 is the largest and it becomes smaller as the activation level increases to 34% and 46%. For all the cells, the capacitance is at its maximum at the lowest current and it drops rapidly as the current increases, quickly arriving on a flat region. This indicates that at the low current end, the major contribution to the capacitance is from micropores. The unit area capacitance in micropores,  $C_{\text{micro}}$ , decreases rapidly with increasing current density, *i.e.*, with increasing charge-discharge rate, while  $C_{\text{ext}}$ , the unit area capacitance from mesopores and bigger pores does not change much, especially in non-aqueous electrolytes.<sup>28,29,35</sup> This is because mesopores can be accessed quickly by charges, whereas the accessibility of micropores is more kinetically limited.

Cycling stability of the capacitors was examined in continuous charge-discharge cycles at a current density of  $25 \text{ mA cm}^{-2}$ . The discharge capacitance data were collected during the GCD cycles, and are shown in Fig. 5. The initial decrease in capacitance is more obvious for carbon materials with higher level of activation, C-34 and C-46, possibly attributed to the charge consumption in some irreversible redox reaction associated with surface functional groups, and with impurities like oxygen and moisture. After the

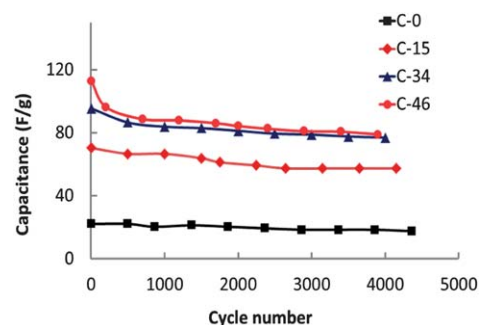


Fig. 5 Specific capacitance vs. the charge-discharge cycling number for C-0, C-15, C-34, and C-46.

initial decrease, the values kept quite stable for a large number of cycles, indicating excellent cycling stability.

Overall, the capacitances of these phenolic resin derived activated carbons are larger than most of the other activated carbons listed in the literature with organic electrolytes,<sup>3,13</sup> and the activation is very effective to promote the material's charge storage capacity through increasing both meso- and micro-pore volumes. C-46 has the highest capacitance among the four carbon samples. It gave a capacitance of  $\sim 160 \text{ F g}^{-1}$  and an energy density of  $\sim 35 \text{ W h kg}^{-1}$  at  $1 \text{ mA cm}^{-2}$  current density, as shown in Fig. 4. Higher capacitance in carbon materials with high activation levels can be expected, but it is not the case that the higher the activation level, the better it is as a supercapacitor electrode, as the increased surface area is mostly attributed to micropores and the contribution of micropores to the capacitance is mainly at low current regions. On the other hand, the capacitance increases with increasing BET surface area,  $S_{\text{BET}}$ , but this increment was reported to be saturated at a  $S_{\text{BET}}$  of above  $1600 \text{ m}^2 \text{ g}^{-1}$ .<sup>36</sup> In highly activated carbon materials, extremely large surface areas correspond to thinner pore walls, space-charge regions begin to overlap and less capacitance is generated per unit electrode area.<sup>37</sup> At high levels of activation, more carbon is burnt off during the activation process and this will increase the production costs. Moreover, at high activation levels, the carbon density reduces, which results in the decrease of volumetric capacitance. It was also found that binding the carbon powder together with PVDF became more and more difficult as the level of activation increased. Thus, more PVDF binder was necessary which impairs the device performance. Therefore, carbon materials with  $\sim 30\%$  activation would be suitable for supercapacitors considering their cost and performance.

## 4 Conclusions

Phenolic resin based activated carbons with different levels of activation were prepared and used to fabricate carbon electrodes for EDLC supercapacitors. The activation process was found to increase the volumes of micropores more rapidly than that of mesopores. The activation was effective to increase the materials' capacitance at lower activation levels and as the level of activation increased, this effect was reduced. Carbon

materials with ~30% activation levels were found to be desirable in terms of their cost and performance, as well as providing high capacitance. The mesopores in the materials provided high capacitances at high charge–discharge rates with organic electrolytes, while the micropores in the materials were the major contributor to the capacitance at the low power end. Both mesopores and micropores were required for high performance EDLC devices. The EDLC cells based on these carbon materials showed quite high cycling stability.

## Acknowledgements

This research was funded by the European Commission FP7 project “AUTOSUPERCAP”.

## Notes and references

- 1 V. Khomenko, E. Raymundo-Pinero and F. Béguin, *J. Power Sources*, 2008, **177**, 643–651.
- 2 A. Burke, *J. Power Sources*, 2000, **91**, 37–50.
- 3 Y. Zhang, H. Feng, X. Wu, L. Wang, A. Zhang, T. Xia, H. Dong, X. Li and L. Zhang, *Int. J. Hydrogen Energy*, 2009, **34**, 4889–4899.
- 4 L. L. Zhang and X. S. Zhao, *Chem. Soc. Rev.*, 2009, **38**, 2520–2531.
- 5 A. Burke, *Electrochim. Acta*, 2007, **53**, 1083–1091.
- 6 C. Lei, P. Wilson and C. Lekakou, *J. Power Sources*, 2011, **196**, 7823–7827.
- 7 K. Naoi and M. Morita, *The Electrochemical Society Interface Spring*, 2008, p44.
- 8 H. E. Katz, P. C. Searson and T. O. Poehler, *J. Mater. Res.*, 2010, **25**, 1561–1574.
- 9 M. Jayalakshmi and K. Balasubramanian, *Int. J. Electrochem. Sci.*, 2008, **3**, 1196–1217.
- 10 C.-C. Hu, C.-C. Wang, F.-C. Wu and R.-L. Tseng, *Electrochim. Acta*, 2007, **52**, 2498–2505.
- 11 A. Tanimura, A. Kovalenko and F. Hirata, *Chem. Phys. Lett.*, 2003, **378**, 638–646.
- 12 K. Nakagawa, S. R. Mukai, K. Tamura and H. Tamon, *Chem. Eng. Res. Des.*, 2007, **85**, 1331–1337.
- 13 M. Inagaki, H. Konno and O. Tanaike, *J. Power Sources*, 2010, **195**, 7880–7903.
- 14 N. Amini, K. F. Aguey-Zinsou and Z. X. Guo, *Carbon*, 2011, **49**, 3857–3864.
- 15 A. Szczurek, K. Jurewicz, G. Amaral-Labat, V. Fierro, A. Pizzi and A. Celzard, *Carbon*, 2010, **48**, 3874–3883.
- 16 S. L. Candelaria, Y. Shao, W. Zhou, X. Li, J. Xiao, J. G. Zhang, Y. Wang, J. Liu, J. Li and G. Cao, *Nano Energy*, 2012, **1**, 195–220.
- 17 J. R. Kim, H. C. Boghani, N. Amini, K. F. Aguey-Zinsou, I. Michie, R. M. Dinsdale, A. J. Guwy, Z. X. Guo and G. C. Premier, *J. Power Sources*, 2012, **213**, 382–390.
- 18 S. R. Tennison, *Appl. Catal., A*, 1998, **173**, 289–311.
- 19 R. Xue, J. Yan, X. Liu, Y. Tian and B. Yi, *J. Appl. Electrochem.*, 2011, **41**, 1357–1366.
- 20 M. Nawa, T. Nogami and H. Mikawa, *J. Electrochem. Soc.*, 1984, **131**, 1457–1462.
- 21 K. Chiba, T. Ueda and H. Yamamoto, *Electrochemistry*, 2007, **75**, 668–671.
- 22 Y. Nono, M. Kouzu, K. Takei, K. Chiba and Y. Sato, *Electrochemistry*, 2010, **78**, 336–338.
- 23 S. R. Tennison, O. Kozynchenko, V. Strelko and A. J. Blackburn, Porous Carbons, *US Pat.*, 2008032092, 2008.
- 24 S. Brunauer, P. H. Emmett and E. Teller, *J. Am. Chem. Soc.*, 1938, **60**, 309–319.
- 25 F. Stoeckli, in *Porosity in carbons-characterization and applications*, ed. J. Patrick, Arnold, London, 1995, pp. 67–97.
- 26 E. P. Barrett, L. G. Joyner and P. P. Halenda, *J. Am. Chem. Soc.*, 1951, **73**, 373–380.
- 27 V. M. Gun'ko, O. P. Kozynchenko, V. V. Turov, S. R. Tennison, V. I. Zarko, Y. M. Nychiporuk, T. V. Kulik, B. B. Palyanytsya, V. D. Osovskii, Y. G. Ptushinskii and A. V. Turov, *Colloids Surf., A*, 2008, **317**, 377–387.
- 28 M. Inagaki, *New Carbon Mater.*, 2009, **24**, 193–232.
- 29 L. Wang, M. Fujita and M. Inagaki, *Electrochim. Acta*, 2006, **51**, 4096–4102.
- 30 C. Lei, F. Markoulidis, Z. Ashitaka and C. Lekakou, *Electrochim. Acta*, 2013, **92**, 183–187.
- 31 Y. J. Kim, Y. A. Kim, T. Chino, H. Suezaki, M. Endo and M. S. Dresselhaus, *Small*, 2006, **2**, 339–345.
- 32 A. Izadi-Najafabadi, S. Yasuda, K. Kobashi, T. Yamada, D. N. Futaba, H. Hatori, M. Yumura, S. Iijima and K. Hata, *Adv. Mater.*, 2010, **22**, E235.
- 33 T. Bordjiba, M. Mohamedi and L. H. Dao, *J. Power Sources*, 2007, **172**, 991–998.
- 34 C. Arbizzani, M. Mastragostino and F. Soavi, *J. Power Sources*, 2000, **100**, 164–170.
- 35 H. Yamada, H. Nakamura, F. Nakahara, I. Moriguchi and T. Kudo, *J. Phys. Chem. C*, 2007, **111**, 227–233.
- 36 L.-H. Wang, M. Toyoda and M. Inagaki, *New Carbon Mater.*, 2008, **23**, 111–115.
- 37 A. G. Pandolfo and A. F. Hollenkamp, *J. Power Sources*, 2006, **157**, 11–27.